OPEN ACCESS
OPUS AUGSBURG

Universität Augsburg
Universitätsbibliothek

Electronic and optical properties of metal-doped TiO2 nanotubes: spintronic and photocatalytic applications

Mohamed Mostafa Fadlallah, Ulrich Eckern

Angaben zur Veröffentlichung / Publication details:

Fadlallah, Mohamed Mostafa, and Ulrich Eckern. 2020. "Electronic and optical properties of metal-doped TiO2 nanotubes: spintronic and photocatalytic applications." *New Journal of Physics* 22 (9): 093028. https://doi.org/10.1088/1367-2630/abae87.

Nutzungsbedingungen / Terms of use: **CC BY 4.0**

Dieses Dokument wird unter folgenden Bedingungen zur Verfügung gestellt: / This document is made available under these conditions:
CC-BY 4.0: Creative Commons: Namensnennung
Weitere Informationen finden Sie unter: / For more information see:
https://creativecommons.org/licenses/by/4.0/deed.de

New Journal of Physics
The open access journal at the forefront of physics

Deutsche Physikalische Gesellschaft DPG IOP Institute of Physics

PAPER • OPEN ACCESS

Electronic and optical properties of metal-doped TiO_2 nanotubes: spintronic and photocatalytic applications

To cite this article: Mohamed M Fadlallah and Ulrich Eckern 2020 *New J. Phys.* **22** 093028

View the article online for updates and enhancements.

This content was downloaded from IP address 137.250.129.180 on 02/10/2020 at 05:57

New Journal of Physics
The open access journal at the forefront of physics

Deutsche Physikalische Gesellschaft DPG
IOP Institute of Physics

Published in partnership with: Deutsche Physikalische Gesellschaft and the Institute of Physics

CrossMark

OPEN ACCESS

RECEIVED
18 May 2020

REVISED
28 July 2020

ACCEPTED FOR PUBLICATION
12 August 2020

PUBLISHED
10 September 2020

Original content from this work may be used under the terms of the Creative Commons Attribution 4.0 licence.

Any further distribution of this work must maintain attribution to the author(s) and the title of the work, journal citation and DOI.

PAPER

Electronic and optical properties of metal-doped TiO_2 nanotubes: spintronic and photocatalytic applications

Mohamed M Fadlallah[1,2] **and Ulrich Eckern**[3]

[1] Physics Department, Faculty of Science, Benha University, 13518 Benha, Egypt
[2] Center for Computational Energy Research, Department of Applied Physics, Eindhoven University of Technology, P.O. Box 513, 5600 MB Eindhoven, The Netherlands
[3] Institute of Physics, University of Augsburg, 86135 Augsburg, Germany

E-mail: mohamed.fadlallah@fsc.bu.edu.eg and ulrich.eckern@physik.uni-augsburg.de

Keywords: titania nanotubes, metal-doping, electronic and optical properties, photocatalytic and spintronic applications

Abstract

Due to their characteristic geometry, TiO_2 nanotubes (TNTs), suitably doped by metal-substitution to enhance their photocatalytic properties, have a high potential for applications such as clean fuel production. In this context, we present a detailed investigation of the magnetic, electronic, and optical properties of transition-metal doped TNTs, based on hybrid density functional theory. In particular, we focus on the 3*d*, the 4*d*, as well as selected 5*d* transition-metal doped TNTs. Thereby, we are able to explain the enhanced optical activity and photocatalytic sensitivity observed in various experiments. We find, for example, that Cr- and W-doped TNTs can be employed for applications like water splitting and carbon dioxide reduction, and for spintronic devices. The best candidate for water splitting is Fe-doped TNT, in agreement with experimental observations. In addition, our findings provide valuable hints for future experimental studies of the ferromagnetic/spintronic behavior of metal-doped titania nanotubes.

1. Introduction

Titanium dioxide (TiO_2, titania) nanostructures have seen exciting applications in a number of areas, including batteries [1], sensors [2], sunscreens [3], photovoltaics [4], solar cells [5], biomedicals [6], catalyst supports [7], photocatalytic degradation of pollutants [8], carbon dioxide reduction [9], hydrogen production [10], and water splitting [11]. In addition, doped TiO_2 nanostructures are promising materials for ferromagnetic and spintronic applications [12, 13]. Due to their low cost, natural abundance, high and long-term stability, and human and environmental safety, titania is ubiquitous in daily life, e.g., in papers, inks, pigments [14, 15], toothpaste [16], cosmetics, medications, and food products [17].

In particular, a titania nanotube (TNT) is an effective nano-photocatalyst that directly splits water [18, 19], and degrades environmental pollutants [8] under sunlight. Furthermore, it is used in solar energy conversion [20] due to the good locations of its conduction band (CB) and valence band (VB) edges with respect to hydrogen formation and oxidation energy [21]. Moreover, the highly ordered nanotube geometry and large internal surface area are very useful as a unidirectional electric channel for the photogenerated electrons [22]. However, the bandgap of TNT (3.18–3.23 eV [23, 24]) restricts its applications in photocatalytic processes because of the limited absorption in the visible-light range. Therefore, engineering the bandgap of TNT by dopants to increase its photosensitivity to visible light is a major target in photocatalyst studies. On the other hand, Co- [25] and Ni-doped [26] TNTs can be used as dilute magnetic semiconductors.

Most publications in the field have been concerned with mechanisms that decrease the bandgap of TNTs, and shift the absorption edges towards the visible-light range. Doping is a common method for tuning the bandgap of semiconductors. Experimentally, a large number of doped TNTs was prepared,

© 2020 The Author(s). Published by IOP Publishing Ltd on behalf of the Institute of Physics and Deutsche Physikalische Gesellschaft

e.g., references [27–31]; and theoretical studies, based on density functional theory (DFT), include, e.g., references [32–34].

With respect to magnetic properties, ferromagnetic behavior has been experimentally observed for V- [35], Ni- [26], and Co-doped [25] TNTs. Theoretically, these dopants are found to induce significant magnetic moments and long-range ferromagnetic coupling [36].

In view of the relative simplicity of preparing metal-doped TNTs [37] (M-TNTs), further theoretical studies are highly needed to elucidate systematically the photocatalytic and magnetic properties of such systems. This paper is devoted to such a task, in particular, we present results of a systematic and accurate—based on hybrid DFT—investigation of the structural, electronic, and optical properties of 3*d*, 4*d*, and selected 5*d* metal-doped TNTs, in order to contribute to a better understanding of available experimental results for photocatalytic and spintronic properties, as well as for providing hints for future experiments.

With respect to spintronics application, magnetic sensors and non-volatile magnetic memories are conceivable. As compared to metal-based spintronics, metal-oxide structures are more versatile because of the ability to control the potential variation and spin polarization by external voltages [38]. Several spintronic experiments have been performed for *carbon* nanotubes using a two-terminal spin valve geometry [39, 40]. This experimental setup makes it difficult, however, to separate spin transport from other effects, such as Hall effect, anisotropic magnetoresistance [41], magneto-Coulomb [42] and interference effects [43]. A four-terminal non-local spin valve setup [41, 44, 45] with a single-wall nanotube can separate the spin current from the charge current [46]. Also, there are promising results for one-dimensional perovskite spintronic devices at a temperature lower than room temperature [47] (which is a key issue for commercial applications). Difficulties in device fabrication include the interface spin transport, and the positioning of nanowires or nanotubes with respect to the other components. The development of the system architecture may help overcome the difficulties associated with traditional electronics, and allow to develop one-dimensional spintronics technologies with good scalability, and lower power dissipation [38].

The details of the calculational approach are given in section 2. In section 3, we address the structural and magnetic properties. The main part of this study, the electronic structures of M-TNTs, is presented in section 4, followed by the optical and photocatalytic properties in section 5. A brief summary is given in section 6.

2. Computational details

All the calculations were carried out using plane-wave pseudopotentials in the Vienna *ab initio* simulation package [48]. Spin-polarized calculations were employed to determine the structural, electronic, and magnetic properties. The generalized gradient approximation in the scheme of Perdew–Burke–Ernzerhof was used as an exchange–correlation functional for structure optimization. The plane-wave functions with cutoff energy 550 eV and $1 \times 1 \times 3$ *k*-mesh based on the Monkhorst–Pack method were utilized to obtain a converged force of 0.01 eV Å^{-1}, and the total tolerance energy is 10^{-6} eV. A periodic supercell along the tube axis (*z* axis) was considered with a vacuum distance of 20 Å between nanotubes in *x* and *y* directions to prevent the interaction between the neighboring TNTs. The convergence of the results was not affected when the parameters (cutoff energy, supercell size, and *k*-mesh) were increased. The Heyd–Scuseria–Ernzerhof hybrid functional (HSE) [49] was employed to calculate the formation energies, electronic structures, and optical properties.

The exchange-energy functional in the HSE scheme is written as a linear combination of short-range (SR) and long-range (LR) terms. The SR term is a PBE exchange functional ($E_X^{\mathrm{PBE,SR}}(\mu)$) mixed with a certain percentage of the exact exchange Hartree–Fock ($E_X^{\mathrm{HF,SR}}(\mu)$) contribution, while the LR term is defined by the PBE exchange functional ($E_X^{\mathrm{PBE,LR}}(\mu)$). The range-separation (screening) parameter μ is usually and also in this work chosen to be 0.2 Å^{-1}. Therefore the exchange–correlation energy functional reads:

$$E_x^{\mathrm{HSE}} = aE_x^{\mathrm{HF,SR}}(\mu) + (1-a)E_x^{\mathrm{PBE,SR}}(\mu) + E_x^{\mathrm{PBE,LR}}(\mu), \tag{1}$$

where *a* is the called exchange mixing coefficient. The standard choice of *a* in the HSE06 package is 25%, but in order to reproduce the experimental TiO_2 bulk bandgap [50], one has to choose a slightly smaller value, 22%. However, both these *a* values strongly overestimate the TNT bandgap. In order to test the sensitivity of the bandgap with respect to variations of the mixing coefficient, we have changed *a* from 10% to 28%: the bandgap is found to be approximately given by 3.0 eV for 10%, and 4.3 eV for 28%, with an almost linear increase in between; cf table 1. The best *a* value, reproducing the experimental TNT bandgap of 3.2 eV, is 14%, which we have chosen in the following. Our results for the DOS (not shown) also indicate

Table 1. TNT bandgap versus mixing parameter a, as calculated with the HSE functional. The experimental value, 3.2 eV, is reproduced for $a = 14\%$. The low value of the optimal mixing parameter for TNT as compared to bulk TiO_2 ($a = 22\%$) means that the electrons in the nanotube are less localized than those in the bulk system, hence the TNT electrons are easily polarizable, implying good screening [51]. This also is an indication that there is no need for more sophisticated many-body techniques like dynamical mean-field theory.

a (%)	10	12	14	16	18	20	22	25	28
Gap (eV)	3.0	3.1	3.2	3.4	3.6	3.7	3.8	4.0	4.3

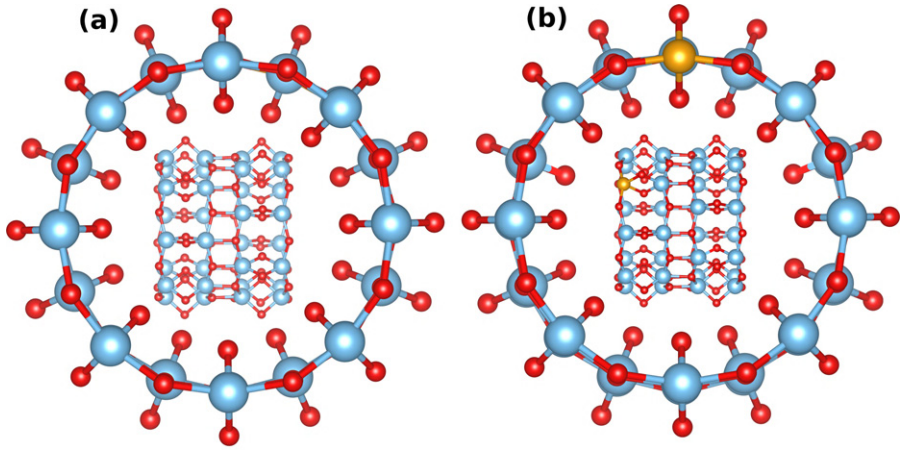

Figure 1. Optimal configurations (top view) of pristine TNT (a) and metal-doped TNT (b), and their side views (small figures). Red, sky-blue, and dark-yellow spheres represent O, Ti, and dopant atom, respectively.

that when increasing a the CB shifts as a whole to higher energy (relative to the Fermi energy), while the VB stays rigid.

The dielectric function, $\varepsilon(\omega) = \varepsilon_1(\omega) + i\varepsilon_2(\omega)$, describes the optical response at the angular frequency ω. First, $\varepsilon_2(\omega)$ is calculated on the basis of the standard golden-rule expression, then $\varepsilon_1(\omega)$ is found by employing the Kramers–Kronig relation. Finally, the absorption spectrum is determined by

$$\alpha(\omega) = \sqrt{2}\,\omega\left(\sqrt{\varepsilon_1^2(\omega) + \varepsilon_2^2(\omega)} - \varepsilon_1(\omega)\right)^{1/2}. \tag{2}$$

3. Stability of M-doped TNTs

TiO_2 anatase nanotubes have been investigated experimentally and theoretically, see, e.g., [52–55], respectively, including details of the geometries and their stabilities [33, 34, 54, 55]. Figure 1(a) illustrates the pristine (8, 0) TNT structure which contains 96 atoms along the tube length (10.49 Å). The cation doped TNT, figure 1(b), is created by replacing a Ti atom by the dopant. The bond length between dopant and Ti atom elongates as the ionic radius of the dopant atom increases for all dopants, as given in tables 2–4. The stability of the metal-doped TNT (M-TNT) is determined from the formation energy (E^{f}):

$$E^{\mathrm{f}} = E^{\mathrm{M-TNT}} + \mu^{\mathrm{Ti}} - (E^{\mathrm{TNT}} + \mu^{\mathrm{M}}), \tag{3}$$

where $E^{\mathrm{M-TNT}}$ and E^{TNT} denote the total energies of metal-doped and pristine TNT, respectively; μ^{Ti} and μ^{M} are the chemical potentials of Ti and the dopant atom, the latter assumed to be given by the energy of the isolated metal atom.

We find the formation energy to be roughly proportional to the number of electrons in the dopant atom, and related to the ionic radius of the larger ions (Sc, Y, La, and Zr). The most stable M-TNT is Ta-TNT because the ionic radius and electronegativity of Ta are very close to the corresponding values of the Ti ion. The formation energies of 4d-TNTs are higher than the corresponding ones in the same group of 3d- and 5d-TNTs, which can be attributed to the large ionic size of 4d dopants as compared to the ionic size of 3d dopants group, and the low electronegativity of 4d dopants as compared to the electronegativity of 5d dopants (tables 2–4).

Regarding the magnetic moment, the difference between the number of outer shell electrons in the metal dopant and the Ti atom determines the magnetic properties of M-TNTs as is apparent, e.g., for Sc- to

Table 2. Ionic radius (Å) (cf [56]), electronegativity (cf [57]), bond lengths (Å), formation energies (E_f (eV)), magnetic moments (μ_B), and bandgap (eV) of selected 3*d*-metal doped TNTs. The pristine system (Ti column) is included for easy reference. The last three rows indicate whether the respective system is useful for spintronic, optical, and photocatalytic applications: the ✓ means 'clear improvement compared to pristine TNT', and the ✗ 'no improvement', w.r.t. that application.

M	Sc	Ti	V	Cr	Mn	Fe	Co	Ni	Cu	Zn
Ionic radius	0.75	0.61	0.54	0.44	0.46	0.78	0.55	0.48	0.54	0.74
Electronegativity	1.36	1.54	1.63	1.66	1.55	1.83	1.88	1.91	1.90	1.65
O–M bond	2.05	1.90	1.89	1.83	1.87	1.88	1.85	1.87	1.96	2.00
E_f	2.91	—	1.55	2.59	3.71	7.18	7.61	9.6	11.90	13.16
Magnetic moment	1.0	0.0	1.0	2.0	3.0	4.0	1.0	0.0	1.0	2.0
Bandgap	2.8	3.2	2.8	2.0	2.5	1.7	1.5	2.0	1.7	2.4
Spintronic	✗	—	✓	✓	✗	✓	✓	✗	✗	✗
Optical	✓	—	✓	✓	✓	✓	✓	✓	✓	✓
Photocatalytic	✗	—	✗	✓	✓	✓	✓	✗	✗	✗

Table 3. Ionic radius (Å) (cf [56]), electronegativity (cf [57]), bond lengths (Å), formation energies (E_f (eV)), magnetic moments (μ_B), and bandgap (eV) of selected 4*d*-metal doped TNTs. The last three rows indicate whether the respective system is useful for spintronic, optical, and photocatalytic applications: the ✓ means 'clear improvement compared to pristine TNT', and the ✗ 'no improvement', w.r.t. that application.

M	Y	Zr	Nb	Mo	Tc	Ru	Rh	Pd	Ag	Cd
Ionic radius	0.90	0.72	0.64	059	0.60	0.68	0.67	0.62	0.75	0.95
Electronegativity	1.22	1.33	1.6	2.16	1.90	2.20	2.28	2.20	1.93	1.69
O–M bond	2.22	2.06	1.96	1.97	1.96	1.96	1.97	1.99	2.11	2.26
E_f	2.90	−1.10	1.03	4.06	5.47	6.79	8.54	11.62	14.05	14.20
Magnetic moment	1.0	0.0	1.0	2.0	1.0	2.0	1.0	0.0	1.0	2.0
Bandgap	2.8	3.2	2.9	2.4	2.5	1.6	1.2	2.2	1.8	2.4
Spintronic	✗	✗	✓	✓	✓	✓	✓	✗	✗	✗
Optical	✓	✗	✓	✓	✓	✓	✓	✓	✓	✓
Photocatalytic	✗	✗	✓	✓	✗	✓	✗	✗	✗	✗

Table 4. Ionic radius (Å) (cf [56]), electronegativity (cf [57]), bond lengths (Å), formation energies (E_f (eV)), magnetic moments (μ_B), and bandgap (eV) of selected 5*d*-metal doped TNTs. The last three rows indicate whether the respective system is useful for spintronic, optical, and photocatalytic applications: the ✓ means 'clear improvement compared to pristine TNT', and the ✗ 'no improvement', w.r.t. that application.

M	La	Ta	W	Pt	Au
Ionic radius	1.03	0.64	0.60	0.63	0.75
Electronegativity	1.1	1.50	2.36	2.28	2.54
O–M bond	2.36	1.92	1.90	2.02	2.2
E_f	2.59	−1.56	1.94	9.08	13.21
Magnetic moment	1.0	1.0	2.0	0.0	1.0
Bandgap	2.8	3.0	2.4	1.8	2.2
Spintronic	✗	✓	✓	✓	✗
Optical	✓	✓	✓	✓	✓
Photocatalytic	✗	✓	✓	✗	✗

Fe-TNTs. For the nearly full outer shell Co, the coupling between the outer shell electrons can explain the magnetic moment of Co-TNT: two outer shell electrons are coupling and the third one is unpaired (low spin state), hence the net magnetic moment is 1 μ_B to a good approximation.

On the other hand, for Co one needs one electron to fill the outer shell, thereby a hole will be created in Co-TNT, and the magnetic moment becomes also 1 μ_B. For the full-filled outer shell atoms (Ni, Cu, and Zn), the magnetic moments are 0 for Ni due to the closed (inert) shell, 1 μ_B for Cu (the oxidation number is (+3)) and a hole is created, and 2 μ_B for Zn (the oxidation number is (+2)) and two holes are created; see table 2. The same trend appears in the 4*d*-TNTs (table 3) except for Tc- and Ru-TNT. As compared to the same atom group (Mn), the magnetic moment for Tc-TNT may be attributed to the low spin state because the coupled states are the same as in Co-TNT. For the Ru doped structure, the magnetic moment is 2 μ_B: two electrons of the outer shell are coupled, the other two are uncoupled (low spin state). From another point of view, two electrons are needed to close the outer shell of Ru so two holes are created in the

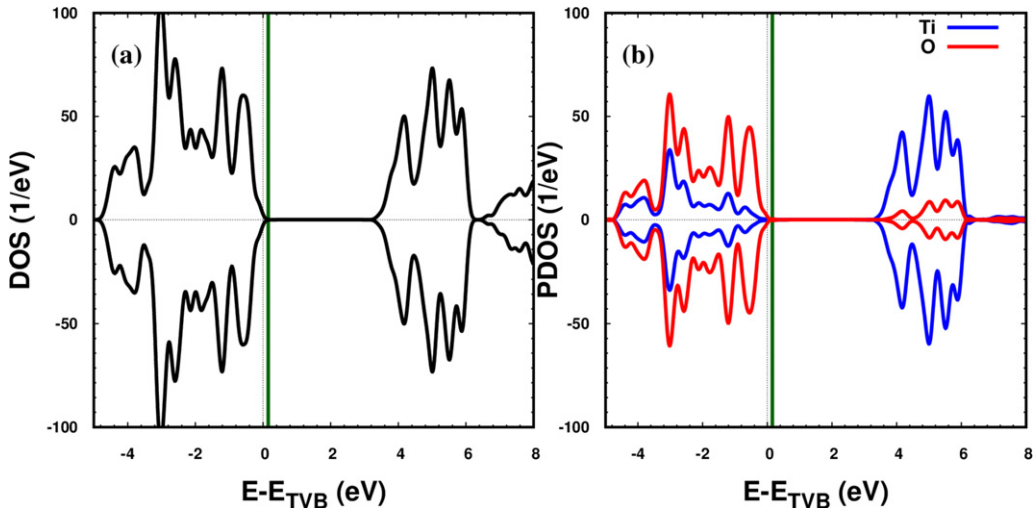

Figure 2. Density of states (DOS) (a), and partial density of states (PDOS) (b), of pristine TNT. The energy is given relative to the top of the valence band (TVB), and the green vertical line indicates the Fermi energy. The overall features of the DOS of pristine TNT, obtained here within *hybrid* DFT, agree well with the result found previously [34] on the basis of DFT within the generalized gradient approximation, provided the 'scissors' operation is applied; see [34] and references therein.

structure, hence the magnetic moment becomes 2 μ_B. For the selected 5*d* dopants, the magnetic moments can be explained by comparison with the above discussed atoms in the *same group* of the periodic table, hence with the same number of outer shell electrons. For example, the Sc, Y, and La dopants (group 3B) have the same magnetic moment of 1 μ_B (table 4).

4. Electronic structure

The DOS and PDOS for pristine TNT are shown in figures 2(a) and (b). The bandgap of 3.20 eV is in good agreement with the experimental bandgap, 3.18–3.23 eV [23, 24] (since we have chosen the mixing parameter, *a*, accordingly, cf section 2). The O states are dominant in the VB, while the Ti states dominate in the CB (figure 2(b)).

In order to structure the presentation, we discuss the electronic structures according to the groups in the periodic table. For 3B group dopants (Sc, Y, La), due to their oxidation number of (+3) as compared to (+4) for Ti, the DOS is asymmetric between the two spin components, and intermediate states are created at 1.1, 0.9, and 1.3 eV for Sc-, Y-, and La-TNTs, respectively. The dopants introduce a hole in the structure. The intermediate states decrease the bandgap to 2.8 eV. As compared to the pristine case, the VBE, the Fermi energy, and the CBEs remain unchanged, see figures 3(a), (c) and (e). The intermediate states are dominated by states from O atoms which are close to the dopant atom; see the PDOSs of the doped structures (figures 3(b), (d) and (f)) and their spin density isosurfaces (respective insets). Note that the reduction in the bandgap may enhance the spectral activity, even though the photocatalytic properties are not being improved due to the location of the intermediate states. In fact, the intermediate states in these doped structures represent recombination centers. Experimentally, Y-TNT was successfully synthesized by a microwave refluxing method, and it was found that the optical activity is increased [28] which indicates a decrease in the bandgap, consistent with our findings.

For the 4B group dopant considered (Zr), the DOS of Zr-TNT has the same DOS as pristine TNT due to the similarity of the Zr and Ti outer shells, so there is no change in the bandgap. The PDOS shows there is no contribution of Zr states in the bandgap and at the band edges (figures 3(g) and (h)).

Since the dopants of the 5B group (V, Nb, Ta) have an additional electron compared to Ti, an asymmetric behavior of the two spin components of the DOS arises. The additional states in the bandgap are located at 1.9 eV for V-TNT, and at the edge of the CB for Nb- and Ta-TNTs (figures 4(a), (c) and (e)). The bandgaps are 2.8, 2.9, and 3.0 eV for V-, Nb-, and Ta-dopants, respectively. The contributions of V (dopant) states to the midgap states are significant in V-TNT, while for Nb- and Ta-TNTs the generated states derive from the Ti (host) states, see figures 4(b), (d) and (f). The V dopant increases the optical activity of pristine TNT without any improvement in the photocatalytic properties due to the position of the midgap states. The generated states at the bottom of the CB, due to Nb and Ta, slightly extend the optical absorption range, enhance the photocatalytic efficiency, and increase the conductivity. Experimental

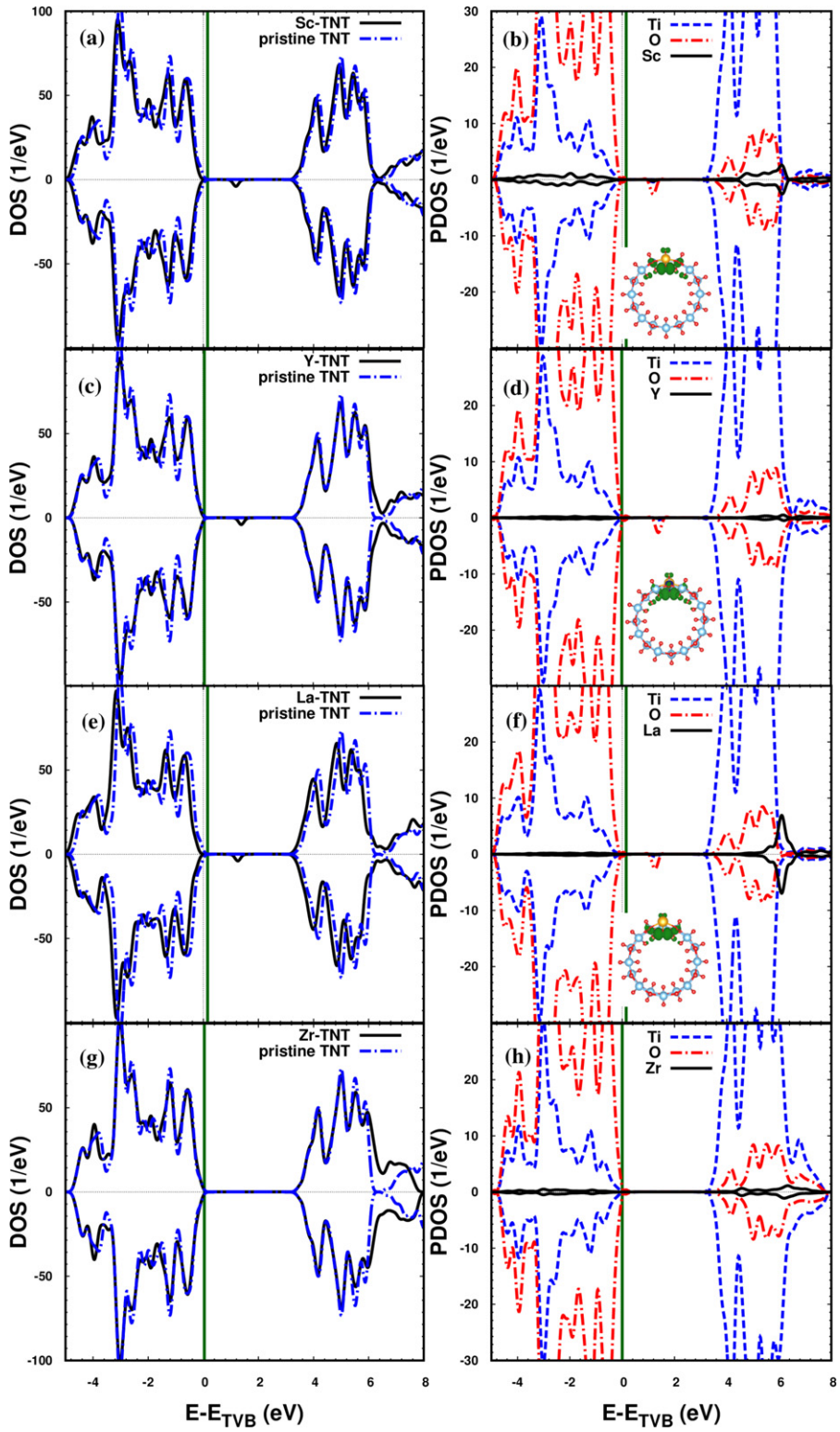

Figure 3. DOS and PDOS for Sc- (a) and (b), Y- (c) and (d), La- (e) and (f), and Zr-doped (g) and (h) TNTs. The energy is given relative to the TVB, and the green vertical line indicates the Fermi energy. The inset figures show the corresponding spin density isosurfaces.

results indeed have shown that V and Nb dopants decrease the bandgap of pristine TNT [27], and of thin films [58]. It is worth mentioning that the reduced bandgap of TNT due to doping with Nb is very similar to the reduced bandgap of TiO_2 thin films with the same dopant, namely 0.3 eV. Furthermore, the experiments observed that Nb-TNT is an n-type conductor [29], consistent with our results. Also, it was found experimentally that Nb [59] and Ta [60] dopings enhance the photocatalytic activity of TNT for water splitting. In addition, ferromagnetic behavior was reported for V-TNT [35]. Clearly, due to the

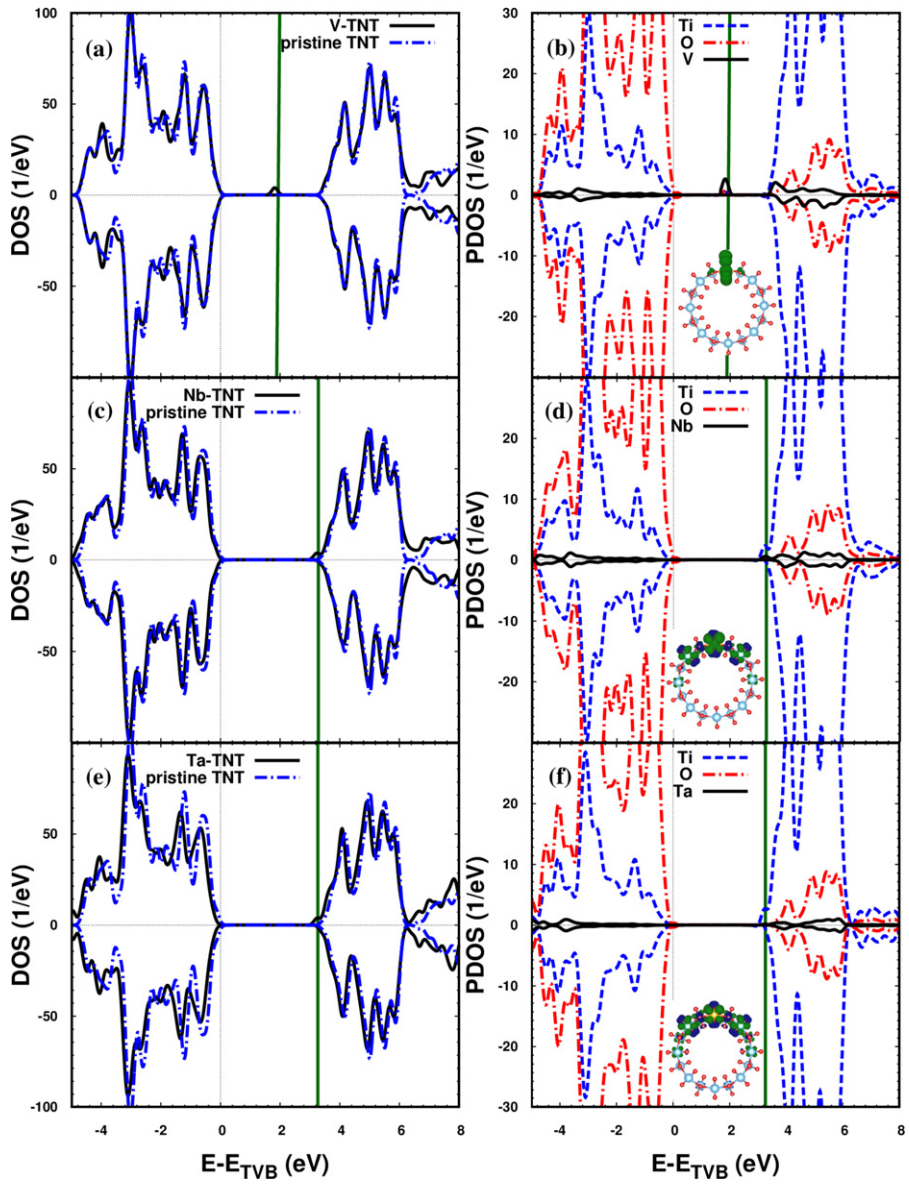

Figure 4. DOS and PDOS for V- (a) and (b), Nb- (c) and (d), and Ta-doped (e) and (f) TNTs. The energy is given relative to the TVB, and the green vertical line indicates the Fermi energy. The inset figures show the corresponding spin density isosurfaces.

metallic spin-up states of Nb- and Ta-TNTs at the Fermi energy, these systems may be useful for spintronic applications.

For the next group, 6B (Cr, Mo, W), there are two additional electrons from the dopants which again implies an asymmetry in the spin resolved DOS (figures 5(a), (c) and (e)). The extra states in the bandgap are created in the range of 0.5–1.3 eV, and below the CBE for Cr-TNT. The generated states appear at 2.7 eV for Mo-TNT, and below the CBE for W-TNT. The gaps of Cr-, Mo-, and W-TNTs are 2.0, 2.4, and 2.4 eV, respectively. The doping with Cr and W improves the optical and photocatalytic activities under visible light irradiation, due to the positions of the states generated within their gaps. For the Cr dopant, the created states are close to the VB and below the CB, therefore the probability of creating a trapping center is small [61]. The locations of the intermediate states for the Mo dopant increases the optical activity as compared to the pristine case. Experimentally, an enhancement of the photocatalytic activity for Cr-TNT [62] as well as a gap narrowing for Mo-TNT [63] were measured. For W doping, a reduction of the gap of nanoparticles was experimentally found [64]. The created bandgap states are related to the dopant states (figures 5(b), (d) and (f)), and the Fermi energy crosses them for the spin up component, therefore Cr-, Mo-, and W-TNTs can be beneficial for spintronic applications. A ferromagnetic behavior at room temperature was observed for Cr-TNT [65].

Considering the dopants in the 7B group, Mn and Tc (figures 6(a) and (c)), the excess single electron in the doped structures leads again to a spin asymmetry in the DOS, and also decreases the bandgap. The

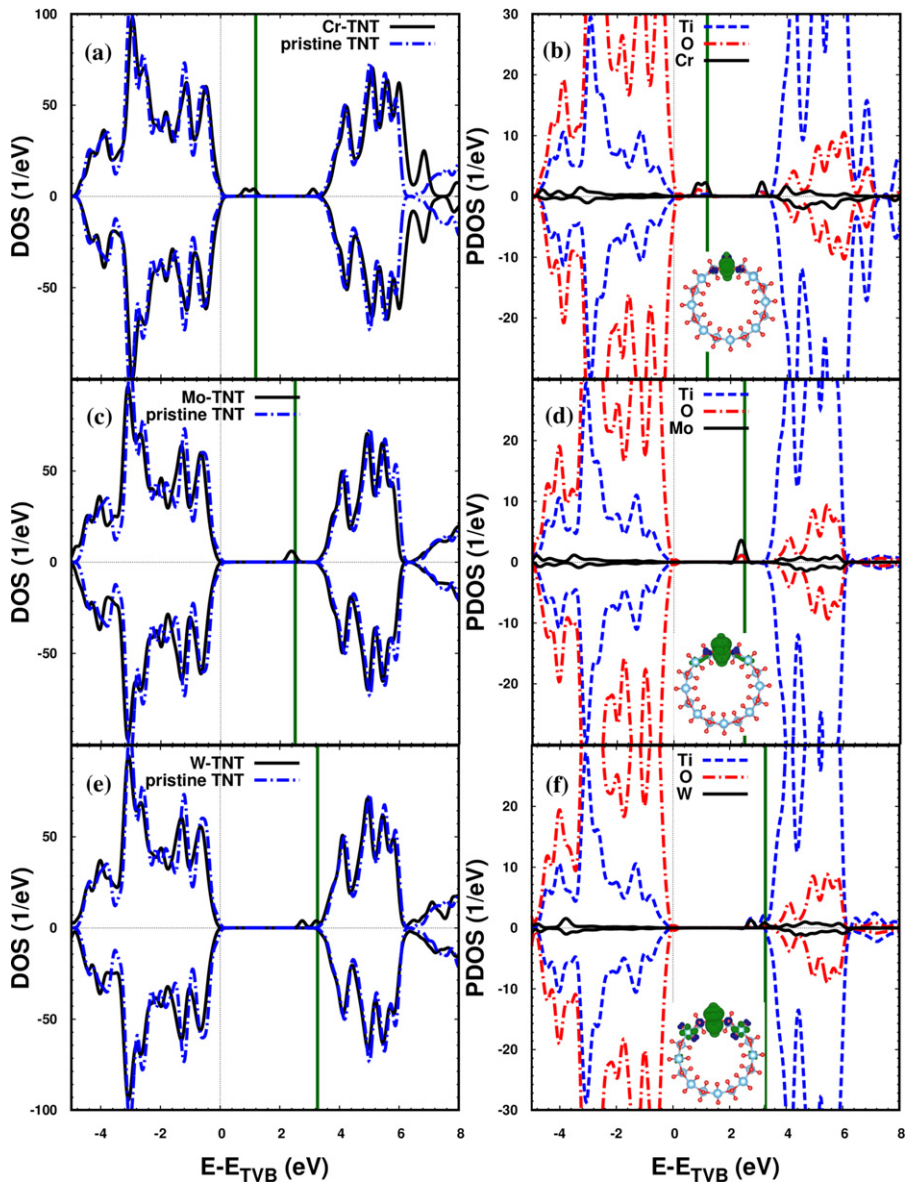

Figure 5. DOS and PDOS for Cr- (a) and (b), Mo- (c) and (d), and W-doped (e) and (f) TNTs. The energy is given relative to the TVB, and the green vertical line indicates the Fermi energy. The inset figures show the corresponding spin density isosurfaces.

created states which appear below the CBE and at 2 eV for Mn-TNT and Tc-TNT, respectively, reduce the bandgap to 2.4 eV for both dopants. Hence Mn and Tc dopings improve the optical properties. The Mn dopant can also enhance the photocatalytic activities due to the location of the created states. This result confirms the experimental observations of the photocatalytic performance for Mn-TNT [66]. Figures 6(b) and (d) show the PDOS of Mn- and Tc-doped TNT; in both cases, the dopant states have their main contributions in the generated states. For Tc-TNT, the spin down midgap states are created at the Fermi energy, so Tc-TNT can be used for spintronic applications. Recently, Tc doped bulk TiO_2 was synthesized [67].

Regarding the 8B group, first two columns (Fe, Ru, Co, Rh), these atoms have nearly full outer shells. As compared to the previous dopants, the created states are more spread inside the bandgap, and appear near the edges of the VB and the CB as well, which implies a stronger reduction of the bandgap (figures 6(e) and (g) and 7(a) and (c)). The bandgaps are 1.7, 1.6, 1.5, and 1.2 eV for Fe-, Ru-, Co-, and Rh-TNTs, respectively. Except for the Rh dopant, all of them will be good candidates for enhancing the optical and photocatalytic activities of TNT. For Fe doping, an improvement of the photocatalytic activity was found experimentally [29, 68]. Also Ru-TNT showed a reduced bandgap as compared to TNT in an experiment [31]. Strong contributions of dopant states exist in the midgap states at the band edges, as shown in the PDOS and the corresponding isosurfaces spin (figures 6(f) and (h) and 7(b) and (d)). Furthermore, the Fermi energy is located inside a portion of the created states for one spin component, therefore such doped

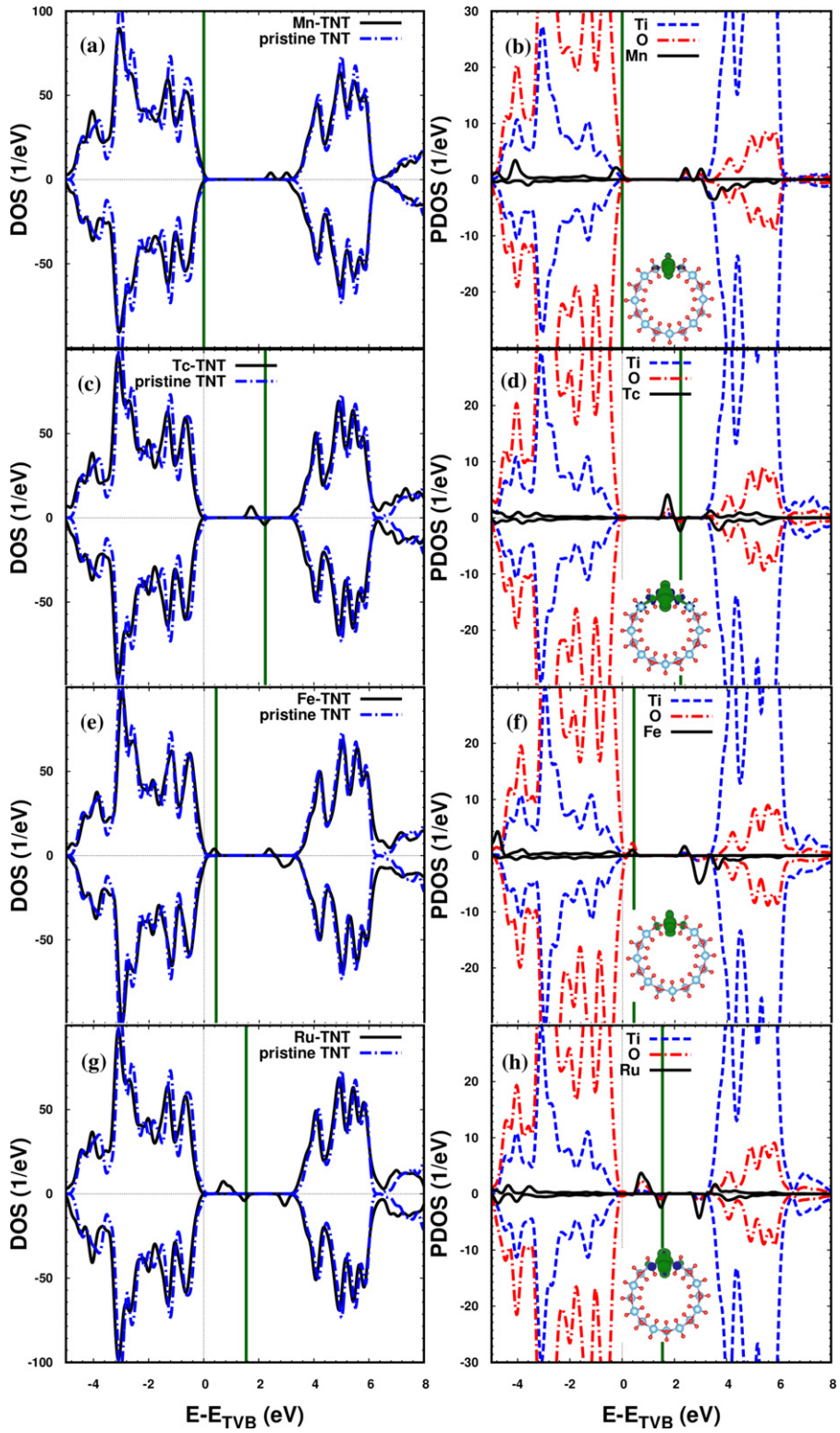

Figure 6. DOS and PDOS for Mn- (a) and (b), Tc- (c) and (d), Fe- (e) and (f), and Ru-doped (g) and (h) TNTs. The energy is given relative to the TVB, and the green vertical line indicates the Fermi energy. The inset figures show the corresponding spin density isosurfaces.

TNTs can be used in spintronic applications. We note that ferromagnetic behavior was experimentally observed for Co-TNT [25].

We turn now to the closed outer shell atoms, namely the last column in the 8B group (Ni, Pd, Pt). The DOS of Ni- and Pd-TNTs are very similar; the intermediate states of Ni-TNT are located near the middle of bandgap. On the other hand, for Pt-TNT they are located at the edges of the VB and the CB (figures 7(e), (g) and (i)). Due to the inert outer shell and zero magnetic moment, the DOS shows a spin-symmetric

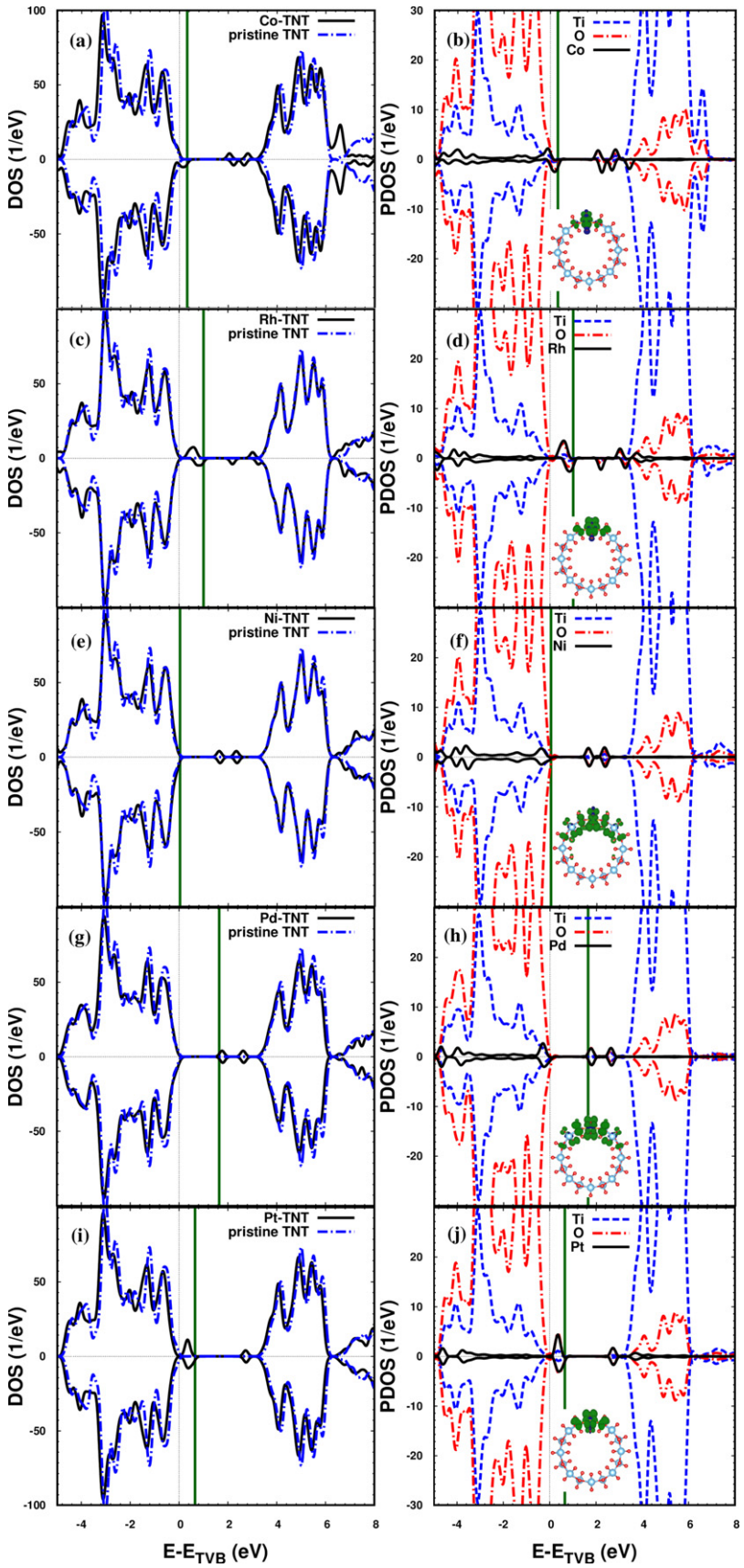

Figure 7. DOS and PDOS for Co- (a) and (b), Rh- (c) and (d), Ni- (e) and (f), Pd- (g) and (h), and Pt-doped (g) and (h) TNTs. The energy is given relative to the TVB, and the green vertical line indicates the Fermi energy. The inset figures show to the corresponding spin density isosurfaces.

behavior. The gaps of those structures are 2.0, 2.2, and 1.8 eV for Ni-, Pd-, and Pt-TNTs, respectively, all of them being smaller than the pristine TNT gap. Figures 7(f), (h) and (j) show the contributions of the Ni,

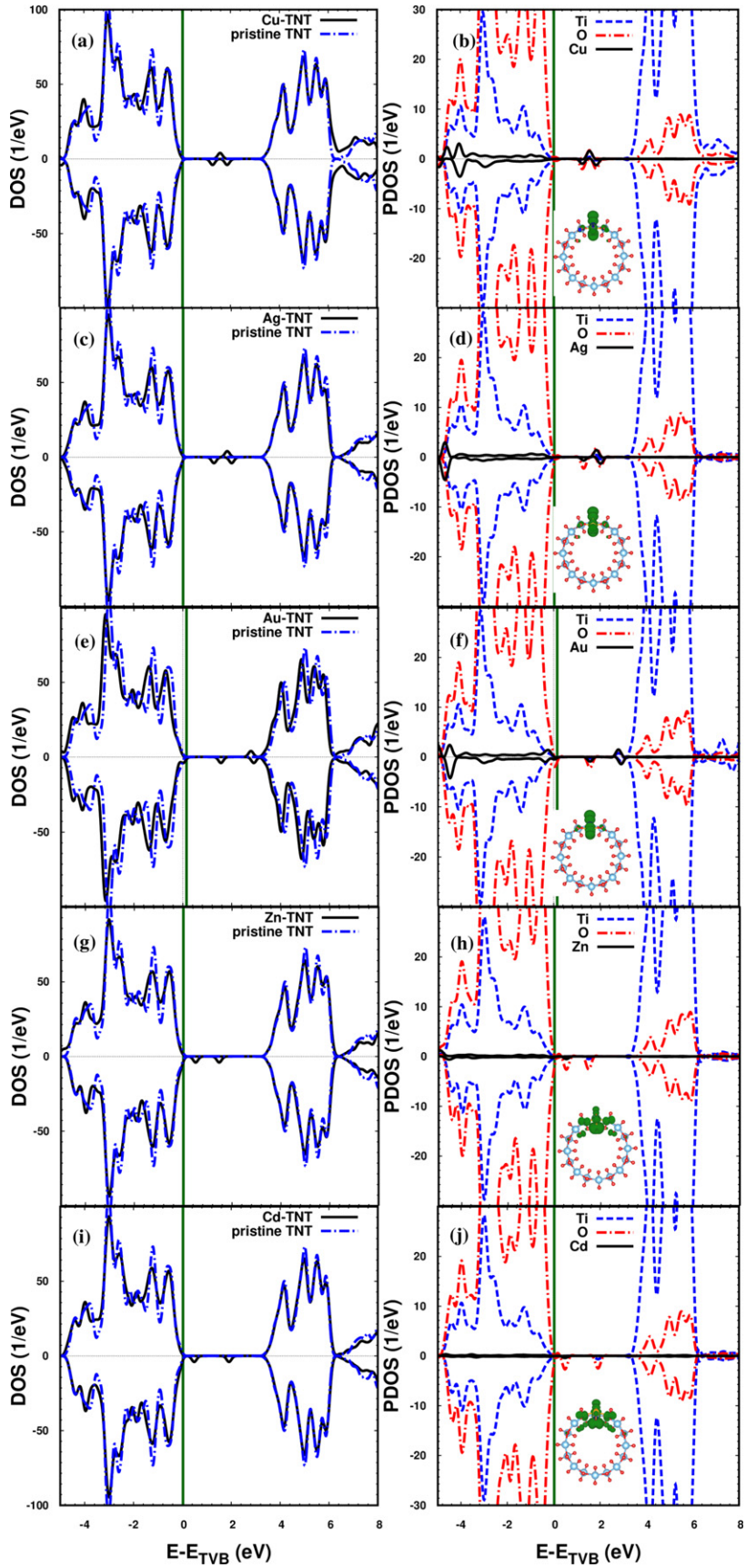

Figure 8. DOS and PDOS for Cu- (a) and (b), Ag- (c) and (d), Au- (e) and (f), Zn- (g) and (h), and Cd-doped (i) and (j) TNTs. The energy is given relative to the TVB, and the green vertical line indicates the Fermi energy. The inset figures show the corresponding spin density isosurfaces.

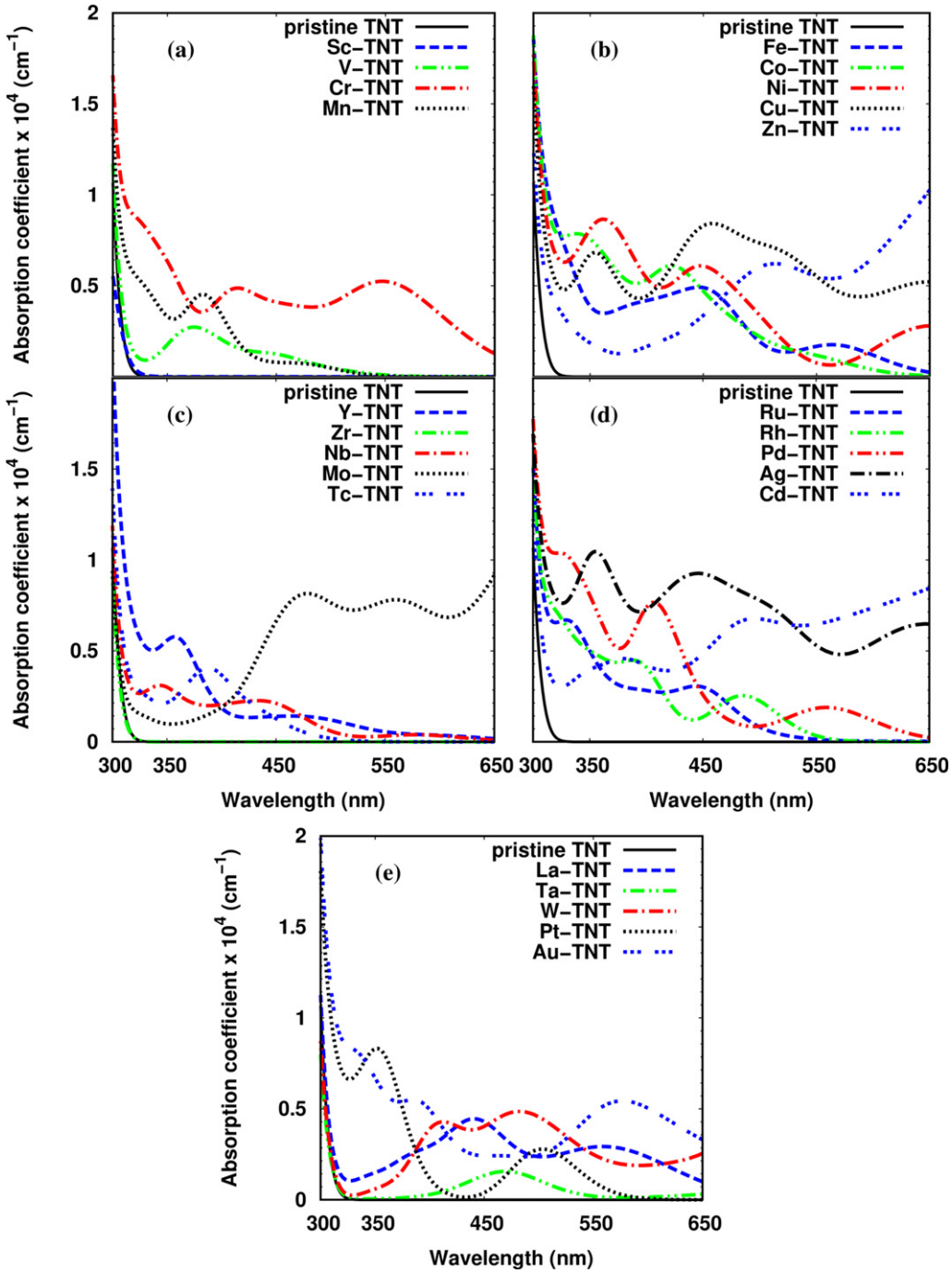

Figure 9. Absorption coefficients for 3*d*- (a) and (b), 4*d*- (c) and (d), and selected 5*d*-doped (e) TNTs.

Pd, and Pt states to the midgap states. Clearly, this group of dopants can improve the optical activity of TNT. But only Pd doping can enhance the photocatalytic activity of TNT due to the contribution of Pd states at the VBE and CBEs. The decrease in the gap of Ni-TNT, as well as of Pd- and Pt-doped nanoparticles, was experimentally reported [69–71].

The next closed outer shell group is 1B (Cu, Ag, Au). The effect of Cu and Ag on the DOS is seen in the midgap states of Cu- and Ag-TNTs, and in the midgap and CBE states for Au-TNT (figures 8(a), (c) and (e)). The bandgap becomes 2.1, 1.8, and 2.2 eV for Cu-, Ag, and Au-TNTs, respectively. Figures 8(b), (d) and (f) show also that the contributions from O atoms surrounding the dopant atoms are stronger than the contributions of the metal dopant states. Although the Fermi energy of Au-TNT crosses the created state, it is not suitable for spintronic applications because the contribution of the O states is dominant. Reduced bandgaps, compared to pristine TNT, have been observed experimentally for Cu- and Ag-TNTs, and for Au doped TiO_2 nanoparticles [29, 71, 72]. This dopant group hence can only improve the optical activity.

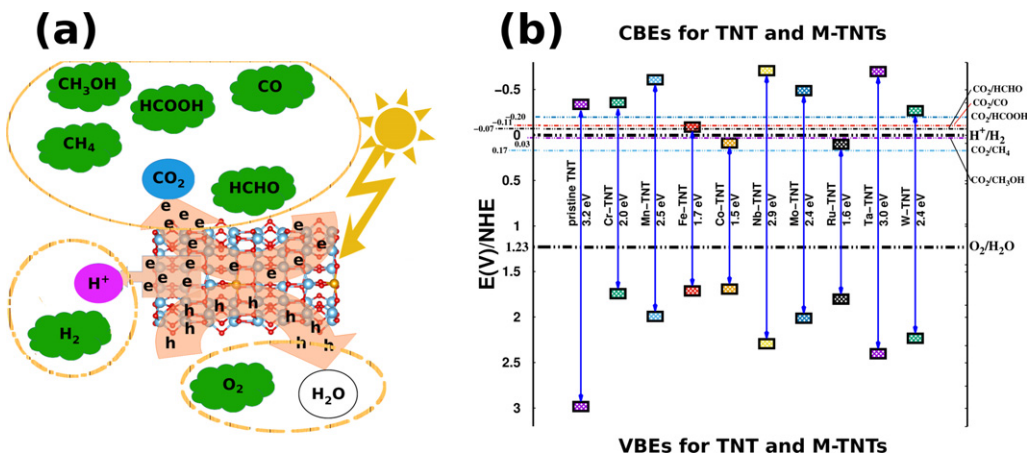

Figure 10. Fundamentals of pristine and M-doped TNTs for photocatalytic water splitting and carbon dioxide reduction for clean fuel production. (a) Schematic overview of concepts and chemical reactions. (b) Summary of band edge positions of the relevant systems. The dashed horizontal lines indicate the water redox and carbon dioxide potentials at pH = 0. The values are given with respect to the NHE (normal hydrogen electrode) potential (in volts).

The last closed outer shell group is 2B (Zn, Cd). The effect of both dopants is the same in the DOS (figures 8(g) and (i)), with a small difference, however, in the location of the created midgap states. Figures 8(h) and (j) show that the midgap states are dominated by contributions from O states. Due to the reduction in the bandgap (2.2 eV for both dopants), Zn and Cd doping can improve the optical activity of pristine TNT, in agreement with experimental results for Zn-TNT [30], and for Cd-doped TiO_2 nanoparticles [73]. The bandgaps and the potential applications (optical, photocatalytic activities, and spintronics) are summarized in tables 2–4.

5. Optical properties and clean fuel production

Figure 9 summarizes the absorption coefficients of pristine, 3*d*-, 4*d*-, and selected 5*d*-TNTs using equation (2). All doped structures show an increase of light absorption, in particular, extending to a wider wavelength range, as compared to the pristine case, except for Sc and Zr. The absorption edge of most M-TNTs is shifted towards lower energy (redshift). Also, additional absorption peaks are observed for M-TNTs in the low energy range. The absorption edge is not only related to the bandgap but also depends on the number of electrons of the dopant: naturally, as the electron number increases the light absorption and its range increase [see, e.g., figure 9(b) as compared to figure 9(a)].

In figure 10(a) we display a schematic figure to elucidate the basic idea of H_2O splitting and CO_2 reduction using M-TNTs as photocatalysts. When M-TNTs absorb light with energy larger than or equal to the bandgap of the photocatalysts (M-TNTs), the electron-hole pairs are separated and migrate to the surface of the photocatalyst, electrons are excited near the CB edge (CBE) and holes are created near the VB edge (VBE). As the bandgap of the photocatalyst decreases, the range of light absorption by M-TNTs increases. During the migration of the photogenerated charges, they may recombine for many reasons, and the number of them will be reduced in the photocatalytic H_2O splitting and CO_2 reduction. The midgap states can be considered as active recombination (trapping) centers for photogenerated charges, so the midgap states are not beneficial.

After the arrival of the photogenerated charge pairs at the M-TNT surface, the photogenerated electrons will reduce the adsorbed H_2O on M-TNT to form H_2 fuel gas, and the photogenerated holes will oxidize H_2O to form O_2 on different active surface sites. Also, the photogenerated electrons can be used to reduce the adsorbed CO_2 on the M-TNTs to several natural fuels (figure 10(a)). The two previous processes can only occur when the CBE is more negative than the H^+ (protons which were produced from the water oxidation process) or CO_2 reduction potentials, and the VBE is more positive than the H_2O oxidation potential. The natural fuel type which can be gained depends on the conditions of the chemical reaction. The detailed mechanisms of H_2O splitting and CO_2 reduction have been reported in several reviews, see, e.g., reference [74].

Figure 10(b) shows the applicability of M-TNTs as catalysts for water splitting and carbon dioxide reduction. For water splitting, as already mentioned in the previous paragraph, the VBE has to be higher (more positive) than the water oxidation potential O_2/H_2O (1.23 eV/NHE), and the CBE has to be lower (more negative) than the redox potential of H^+/H_2 (0 eV/NHE). Therefore, the bandgap of the

photocatalyst has to be larger than 1.23 eV (∼1000 nm) to split water into H_2 and O_2, which is the minimum Gibbs free energy for this process. Here, the band edges are measured with respect to the NHE, and their determination is discussed in detail in many publications, see, e.g., references [33, 34] and references therein. For the CO_2 reduction, the CBE has to be lower (more negative) than the redox potential of the natural fuel/CO_2. The positions of the band edges (which depend on the bandgap) are the main criterion for specifying a good photocatalyst for H_2O splitting or CO_2 reduction.

Figure 10(b) demonstrates that Fe-TNT is best for producing hydrogen (from water splitting), methane, and methanol (from CO_2 reduction). The Co- and Ru-TNTs have the lowest bandgaps, but they are useful photocatalysts for generating methane fuel only. The Cr-TNT is the best candidate for producing all the considered clean fuels in this study. The other M-TNTs in figure 10(b) show photocatalytic activities which enables them to split H_2O and reduce CO_2 reduction better than pristine TNT.

6. Summary

In this work we systematically discussed the electronic, magnetic, and optical properties of TNTs doped with 3*d*, 4*d*, and selected 5*d* transition metals, in order to elucidate their potential for various applications. Our study has been based on hybrid DFT, which is known for leading to most accurate (in comparison to other DFT-based approximations) results. The stability of M-doped TNTs can be understood, to a large extent, in terms of the ionic size and the electronegativity of the metal dopants. The magnetic moments of doped TNTs depend on the number of outer shell *d* electrons of the dopant (up to about half-filling of the outer shell, i.e., for d^1 to d^6), and on the coupling between the outer shell electrons (in particular, for higher fillings, d^7 to d^{10}).

Dopant-related states at the Fermi energy for one spin component are found in several M-doped TNTs (see tables 2–4), giving rise to 'spintronic' properties. The metal dopants, except for Zr, create midgap states which implies a narrowing of the bandgap as compared to the pristine structure. Therefore all M-doped TNTs are more useful for optical applications than pristine TNT. The calculations demonstrate that Mo-doped TNT has the highest optical activity as compared to other doped structures.

The bandgap and the position of the dopant states determine the enhancement of the photocatalytic sensitivity. In particular, Cr-, Mn-, Fe-, Co-, Nb-, Ru-, Ta-, and W-doped TNTs are expected to be preferential for photocatalytic applications (water splitting and carbon dioxide reduction) as compared to pristine TNT. Fe-doped TNT is the best candidate for water splitting and for the production of hydrogen, methane, and methanol fuels, while the Cr- and W-doped TNTs are best for water splitting and CO_2 reduction, i.e., for the production of clean fuels and, at the same time, for helping to decrease the CO_2 pollution. However, in several cases (14 out of 24) the created midgap states prevent an enhancement of photocatalytic sensitivity. Our results compare favorably with available experimental observations.

Acknowledgments

Financial support from the Deutsche Forschungsgemeinschaft (project number 107745057, TRR 80) is gratefully acknowledged.

ORCID iDs

Mohamed M Fadlallah https://orcid.org/0000-0003-2102-1022
Ulrich Eckern https://orcid.org/0000-0001-8917-9083

References

[1] Zhu G-N, Wang Y-G and Xia Y-Y 2012 *Energy Environ. Sci.* **5** 6652
[2] Zarifi M H, Farsinezhad S, Abdolrazzaghi M, Daneshmand M and Shankar K 2016 *Nanoscale* **8** 7466
[3] Salvador A, Pascual-Martí M, Adell J, Requeni A and March J 2000 *J. Pharm. Biomed. Anal.* **22** 301
[4] Liao J-Y, He J-W, Xu H, Kuang D-B and Su C-Y 2012 *J. Mater. Chem.* **22** 7910
[5] He X, Guo Y, Liu J, Li X and Qi J 2019 *J. Power Sources* **423** 236
[6] Fei Yin Z, Wu L, Gui Yang H and Hua Su Y 2013 *Phys. Chem. Chem. Phys.* **15** 4844
[7] Maeda Y, Iizuka Y and Kohyama M 2013 *J. Am. Chem. Soc.* **135** 906
[8] Shen S, Chen J, Wang M, Sheng X, Chen X, Feng X and Mao S S 2018 *Prog. Mater. Sci.* **98** 299
[9] Wei L, Yu C, Zhang Q, Liu H and Wang Y 2018 *J. Mater. Chem.* A **6** 22411
[10] Naldoni A, Altomare M, Zoppellaro G, Liu N, Kment Š, Zbořil R and Schmuki P 2019 *ACS Catal.* **9** 345
[11] Kment Š *et al* 2017 *Chem. Soc. Rev.* **46** 3716

[12] Yamada Y *et al* 2011 *Science* **332** 1065
[13] Matsumoto Y *et al* 2001 *Science* **291** 854
[14] Braun J H, Baidins A and Marganski R E 1992 *Prog. Org. Coat.* **20** 105
[15] Pfaff G and Reynders P 1999 *Chem. Rev.* **99** 1963
[16] Yuan S, Chen W and Hu S 2005 *Mater. Sci. Eng.* C **25** 479
[17] Lu P-J, Huang S-C, Chen Y-P, Chiueh L-C and Shih D Y-C 2015 *J. Food Drug Anal.* **23** 587
[18] Preethi L K and Mathews T 2019 *Catal. Sci. Tech.* **9** 5425
[19] Ge M *et al* 2017 *Adv. Sci.* **4** 1600152
[20] Wang M, Ioccozia J, Sun L, Lin C and Lin Z 2014 *Energy Environ. Sci.* **7** 2182
[21] Smith W A, Sharp I D, Strandwitz N C and Bisquert J 2015 *Energy Environ. Sci.* **8** 2851
[22] Albu S P, Ghicov A, Macak J M, Hahn R and Schmuki P 2007 *Nano Lett.* **7** 1286
[23] Momeni M M and Nazari Z 2016 *Ceram. Int.* **42** 8691
[24] Momeni M M and Ghayeb Y 2015 *J. Electroanal. Chem.* **751** 43
[25] Wang X W, Gao X P, Li G R, Gao L, Yan T Y and Zhu H Y 2007 *Appl. Phys. Lett.* **91** 143102
[26] Patel S K S, Jena P and Gajbhiye N 2019 *Mater. Today: Proc.* **15** 388
[27] Lu D, Zhang M, Zhang Z, Li Q, Wang X and Yang J 2014 *Nanoscale Res. Lett.* **9** 272
[28] Rao J, Xue H, Zhang W, Li X, You X and Xing Z 2016 *Int. J. Electrochem. Sci.* **11** 2408
[29] Alivov Y, Singh V, Ding Y, Cerkovnik L J and Nagpal P 2014 *Nanoscale* **6** 10839
[30] Su C-Y, Wang L-C, Liu W-S, Wang C-C and Perng T-P 2018 *ACS Appl. Mater. Interfaces* **10** 33287
[31] Khan M A, Han D H and Yang O-B 2009 *Appl. Surf. Sci.* **255** 3687
[32] Piskunov S, Lisovski O, Begens J, Bocharov D, Zhukovskii Y F, Wessel M and Spohr E 2015 *J. Phys. Chem.* C **119** 18686
[33] Fadlallah M 2017 *Physica* E **89** 50
[34] Fadlallah M M and Eckern U 2020 *Phys. Status Solidi* B **257** 1900217
[35] Patel S and Gajbhiye N 2011 *Solid State Commun.* **151** 1500
[36] Zhang Y, Jia H, Jia H, Liu H, Cao E and Hu J 2017 *J. Magn. Magn. Mater.* **443** 202
[37] Aijo John K *et al* 2019 *Chem. Phys.* **523** 198
[38] Tian Y, Bakaul S R and Wu T 2012 *Nanoscale* **4** 1529
[39] Kim J-R, So H M, Kim J-J and Kim J 2002 *Phys. Rev.* B **66** 233401
[40] Zhao B, Mönch I, Mühl T, Vinzelberg H and Schneider C M 2002 *J. Appl. Phys.* **91** 7026
[41] Jedema F J, Filip A T and van Wees B J 2001 *Nature* **410** 345
[42] van der Molen S J, Tombros N and van Wees B J 2006 *Phys. Rev.* B **73** 220406
[43] Man H T and Morpurgo A F 2005 *Phys. Rev. Lett.* **95** 026801
[44] Johnson M and Silsbee R H 1985 *Phys. Rev. Lett.* **55** 1790
[45] Jedema F J, Heersche H B, Filip A T, Baselmans J J A and van Wees B J 2002 *Nature* **416** 713
[46] Tombros N, van der Molen S J and van Wees B J 2006 *Phys. Rev.* B **73** 233403
[47] Li L, Liang L, Wu H and Zhu X 2016 *Nanoscale Res. Lett.* **11** 121
[48] Kresse G and Joubert D 1999 *Phys. Rev.* B **59** 1758
[49] Heyd J, Scuseria G E and Ernzerhof M 2003 *J. Chem. Phys.* **118** 8207
[50] Çelik V and Mete E 2012 *Phys. Rev.* B **86** 205112
[51] Marques M A L, Vidal J, Oliveira M J T, Reining L and Botti S 2011 *Phys. Rev.* B **83** 035119
[52] Yao B D, Chan Y F, Zhang X Y, Zhang W F, Yang Z Y and Wang N 2003 *Appl. Phys. Lett.* **82** 281
[53] Varghese O K, Gong D, Paulose M, Grimes C A and Dickey E C 2003 *J. Mater. Res.* **18** 156
[54] Bandura A and Evarestov R 2009 *Surf. Sci.* **603** L117
[55] Szieberth D, Ferrari A M, Noel Y and Ferrabone M 2010 *Nanoscale* **2** 81
[56] Shannon R D 1976 *Acta Crystallogr.* A **32** 751
[57] James A M and Lord M P 1992 *Macmillan's Chemical and Physical Data* (London: Macmillan)
[58] Uyanga E, Gibaud A, Daniel P, Sangaa D, Sevjidsuren G, Altantsog P, Beuvier T, Lee C H and Balagurov A 2014 *Mater. Res. Bull.* **60** 222
[59] Das C, Roy P, Yang M, Jha H and Schmuki P 2011 *Nanoscale* **3** 3094
[60] Altomare M, Lee K, Killian M S, Selli E and Schmuki P 2013 *Chem. Eur. J.* **19** 5841
[61] Liu J, Weng M, Li S, Chen X, Cen J, Jie J, Xiao W, Zheng J and Pan F 2020 *Phys. Chem. Chem. Phys.* **22** 39
[62] Zhang S, Chen Y, Yu Y, Wu H, Wang S, Zhu B, Huang W and Wu S 2008 *J. Nanopart. Res.* **10** 871
[63] Feng F, Yang W, Gao S, Sun C and Li Q 2018 *ACS Sustain. Chem. Eng.* **6** 6166
[64] Liu X, Shi Y, Dong Y, Li H, Xia Y and Wang H 2017 *New J. Chem.* **41** 13382
[65] Liao Y, Zhang H, Li J, Yu G, Zhong Z, Bai F, Jia L, Zhang S and Zhong P 2014 *J. Appl. Phys.* **115** 17C304
[66] Xu Z, Li C, Fu N, Li W and Zhang G 2018 *J. Appl. Electrochem.* **48** 1197
[67] Lukens W W and Saslow S A 2017 *Chem. Mater.* **29** 10369
[68] Sun L, Li J, Wang C, Li S, Chen H and Lin C 2009 *Sol. Energy Mater. Sol. Cells* **93** 1875
[69] Dong Z, Ding D, Li T and Ning C 2018 *Appl. Surf. Sci.* **443** 321
[70] Lee H, Shin M, Lee M and Hwang Y J 2015 *Appl. Catal. B: Environ.* **165** 20
[71] Rupa A V, Divakar D and Sivakumar T 2009 *Catal. Lett.* **132** 259
[72] Wang Y, Li Z, Tian Y, Zhao W, Liu X and Yang J 2014 *Mater. Lett.* **122** 248
[73] Chen C-Y, Wei T-C and Li J-Y 2017 *ChemistrySelect* **2** 3648
[74] Xie S, Zhang Q, Liu G and Wang Y 2016 *Chem. Commun.* **52** 35